

Wave mode coupling due to plasma wakes in two-dimensional plasma crystals: In-depth view

L. Couëdel,^{1,2} S. K. Zhdanov,¹ A. V. Ivlev,^{1, a)} V. Nosenko,¹ H. M. Thomas,¹ and G. E. Morfill¹

¹⁾Max Planck Institute for Extraterrestrial Physics, 85741 Garching, Germany

²⁾PIIM, CNRS/Université de Provence, 13397 Marseille Cedex 20, France

Experiments with two-dimensional (2D) plasma crystals are usually carried out in rf plasma sheaths, where the interparticle interactions are modified due to the presence of plasma wakes. The wake-mediated interactions result in the coupling between wave modes in 2D crystals, which can trigger the mode-coupling instability and cause melting. The theory predicts a number of distinct fingerprints to be observed upon the instability onset, such as the emergence of a new hybrid mode, a critical angular dependence, a mixed polarization, and distinct thresholds. In this paper we summarize these key features and provide their detailed discussion, analyze the critical dependence on experimental parameters, and highlight the outstanding issues.

PACS numbers: 52.27.Lw, 52.27.Gr

I. INTRODUCTION

Stability of two-dimensional (2D) plasma crystals is a fundamental problem of complex (dusty) plasmas. Such crystals – which are monolayers of hexagonally ordered monodisperse microparticles – can be (routinely) created in a rf plasma^{1,2}: Particles get negatively charged in a plasma and therefore the electric force exerted on them in the sheath above a horizontal electrode can compensate for gravity, thus providing a stable levitation. There are several mechanisms operating in complex plasmas that can result in the melting of 2D crystals. These mechanisms can generally be divided into two categories – *generic* and *plasma-specific*.

Generic mechanisms of melting are those operating in any (classical) system with a given pair interaction between particles, provided the interaction can be described by a Hamiltonian. The melting in 2D systems can either be a two-step process (which involves consecutive unbinding of weakly interacting dislocation and disclination pairs, respectively, with the intermediate hexatic phase)^{3–6} or a one-step process (where the hexatic phase is preempted by the formation of dislocation chains)⁷. These generic melting mechanisms can operate in very different 2D systems including complex plasmas^{8–13}.

Plasma-specific melting mechanisms can only operate in complex plasmas. Such mechanisms are associated with the energy exchange between microparticles and ambient plasma and can be considered as a result of the system openness. For instance, 2D plasma crystals can be strongly perturbed by single particles moving above or below the monolayer^{14,15}, or they can melt due to fluctuations of particle charges^{16–18}.

The most universal among the plasma-specific mechanisms is that associated with the *wake-mediated* interaction between microparticles: In the presence of strong plasma flow the screening cloud around each charged particle becomes highly asymmetric^{19–22}. These clouds are

usually referred to as “plasma wakes”^{23–27} and play the role of a “third body” in the interparticle interaction, making it nonreciprocal²⁸. Under certain conditions, this makes the system non-Hamiltonian and provides effective conversion of the energy of flowing ions into the kinetic energy of microparticles^{1,2,29,30}.

The wake-induced mechanism of melting of crystalline monolayers was discovered theoretically a decade ago by Ivlev and Morfill³¹. Based on a simple model of a particle chain, it was shown that the longitudinal in-plane and transverse out-of-plane dust-lattice (DL) wave modes are no longer independent – they are coupled due to the wake-mediated interactions. When the modes intersect they become modified by the coupling and form a *hybrid* mode in a narrow vicinity of the crossing. This can trigger the *mode-coupling instability* which causes the melting. This melting mechanism had received strong confirmation later on, when the instability threshold predicted by the theory was compared³² with the experimental observations by U. Konopka and numerical simulations by G. Joyce. However, the direct comparison of theory and experiment became possible only recently, after an experimental method of measuring the out-of-plane mode was developed³³ and therefore the essential fingerprint of the mode-coupling instability – the hybrid mode – became observable. In recent experiment by Couëdel *et al.*³⁴ an implementation of this method unambiguously demonstrated that the melting indeed occurs due to the resonance coupling between the longitudinal in-plane and transverse out-of-plane modes. The variation of the wave modes with the experimental conditions, including the emergence of the hybrid branch, revealed exceptionally good agreement with the theory of mode-coupling instability generalized for 2D case by Zhdanov *et al.*³⁵.

The theory of mode-coupling instability^{31,32,35} predicts a number of distinct fingerprints to be observed upon the instability onset: Along with the emergence of hybrid mode mentioned above, these are a critical angular dependence – the hybrid mode first appears only for wave vectors oriented along one of the principal lattice axes, a mixed polarization – the two DL modes that form the

^{a)}Electronic mail: ivlev@mpe.mpg.de

hybrid mode are no longer purely longitudinal and transverse close to the merging point, and distinct thresholds – the instability sets in only when (i) the particle number density in the monolayer is high enough or/and vertical confinement eigenfrequency is low enough (so that the two DL modes can cross and form the hybrid mode) and (ii) the gas pressure is low enough (so that the growth rate of the hybrid mode exceeds the damping rate).

All these fingerprints have been mentioned in our previous theoretical publications^{31,32,35}, some of them were also illustrated in the followup experimental paper³⁴. However, their discussion was apparently too concise to address all these important properties in necessary detail. The need for in-depth discussion of the wake-mediated mode coupling became evident now, when new publications have appeared where some essential properties of the instability were misinterpreted (see, e.g., recent experimental paper³⁶ and the subsequent Erratum³⁷ by Liu *et al.*). Therefore, in this paper we summarize the key features of the mode coupling and provide a detailed discussion, analyze the critical dependence on experimental parameters, and highlight the outstanding issues.

II. SUMMARY OF MODE-COUPLING THEORY

In 2D plasma crystals, two in-plane wave modes can be sustained (here we naturally leave aside polydisperse mixtures). Both modes have an acoustic dispersion, one of them is longitudinal and the other is transverse. Since the strength of the vertical confinement in such systems is finite, there is a third fundamental wave mode which has an optical dispersion and is associated with the out-of-plane oscillations^{31,35,38–42}. Theory predicts that all three modes depend critically on the parameters of the plasma wakes. Yet the role of the wakes is not only the modification of the modes themselves. What is far more important is that the modes are *coupled* to each other due to the wake-mediated interactions between particles. It is worth noting that this *coupling is linear* and therefore does not depend on the wave amplitude. Below we identify the conditions when the wake-mediated coupling becomes crucial for waves in 2D crystals.

A. DL modes for nonreciprocal interactions

In general, linear dispersion relations $\omega(\mathbf{k})$ are determined by eigenvalues (eigenmodes) of a dynamical matrix \mathbf{D} . The latter is derived by considering small perturbations of individual particles (with respect to a stable configuration, e.g., a hexagonal monolayer for 2D crystals) of the form $\propto \exp(-i\omega t + i\mathbf{k} \cdot \mathbf{r})$. Elements of \mathbf{D} are determined by properties of interparticle interactions and are functions of \mathbf{k} . If the interactions are reciprocal then \mathbf{D} is Hermitian, and therefore the eigenvalues are always real (i.e., the modes are stable) and the eigenvectors are orthogonal. The situation changes if the interactions are

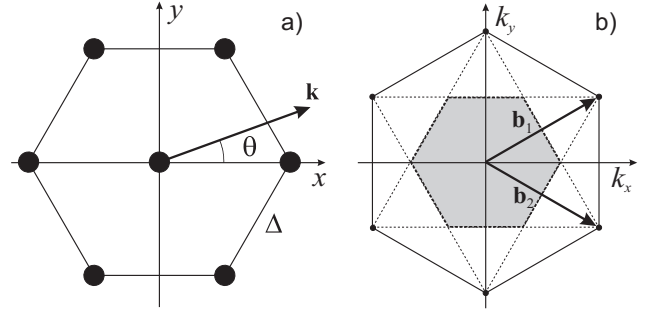


FIG. 1. (a) Elementary hexagonal lattice cell with the frame of reference, the lattice constant is Δ . (b) The reciprocal lattice in \mathbf{k} -space, the basis vectors of the lattice are $\mathbf{b}_{1,2} = 2\pi\Delta^{-1}(1, \pm\frac{1}{\sqrt{3}})$. Due to the lattice symmetry, it is sufficient to consider the wave vectors \mathbf{k} at $0^\circ \leq \theta \leq 30^\circ$ and from within the first Brillouin zone (gray region enclosed by dashed lines), so that $|\mathbf{k}|\Delta \leq \frac{4}{3}\pi$ for $\theta = 0^\circ$ and $|\mathbf{k}|\Delta \leq \frac{2}{\sqrt{3}}\pi$ for $\theta = 30^\circ$.

nonreciprocal – the eigenvalues in this case can become complex.

Before specifying a particular functional form of interparticle interactions in 2D crystals, let us generally assume the non-reciprocity and discuss common properties of the DL waves in this case. The dynamical matrix has the following form:

$$\mathbf{D} = \begin{pmatrix} \alpha_h - \beta & 2\gamma & i\sigma_y \\ 2\gamma & \alpha_h + \beta & i\sigma_x \\ i\sigma_y & i\sigma_x & \Omega_{\text{conf}}^2 - 2\alpha_v \end{pmatrix}. \quad (1)$$

The elements $\alpha_h(\mathbf{k})$, $\beta(\mathbf{k})$, and $\gamma(\mathbf{k})$ determine the dispersion of two in-plane (horizontal) modes and $\alpha_v(\mathbf{k})$ characterizes the out-of-plane (vertical) mode. The elements $\sigma_{x,y}(\mathbf{k})$ emerge due to non-reciprocity and make \mathbf{D} non-Hermitian. The matrix is calculated for the reference frame shown in Fig. 1(a) assuming that vertically the particles are confined in a (parabolic) potential well characterized by the eigenfrequency $\Omega_{\text{conf}} = 2\pi f_{\text{conf}}$. To derive the dispersion relations $\omega(\mathbf{k})$, we add a friction force $m\nu\dot{\mathbf{r}}$ in equations of motion (with ν being the damping rate) which yields:

$$\det[\mathbf{D} - \omega(\omega + i\nu)\mathbf{I}] = 0, \quad (2)$$

where \mathbf{I} is the unit matrix. Thus, $\omega(\omega + i\nu) \equiv \Omega^2$ are the eigenvalues of \mathbf{D} , i.e., the DL wave modes.

For reciprocal interactions $\sigma_{x,y} = 0$ and then Eqs (1) and (2) yield

$$(\Omega^2 - \Omega_{h\parallel}^2)(\Omega^2 - \Omega_{h\perp}^2)(\Omega^2 - \Omega_v^2) = 0. \quad (3)$$

There are three independent and real DL modes: Two *acoustic* in-plane modes $\Omega^2(\mathbf{k}) = \alpha_h \pm \sqrt{\beta^2 + 4\gamma^2} \equiv \Omega_{h\parallel,\perp}^2(\mathbf{k})$ (where \parallel and \perp indicate the longitudinal and transverse polarizations and correspond to the plus and minus signs, respectively) and an *optical* out-of-plane

mode $\Omega^2(\mathbf{k}) = \Omega_{\text{conf}}^2 - 2\alpha_v \equiv \Omega_v^2(\mathbf{k})$. When solved for $\omega(\mathbf{k})$, each mode yields a couple of conjugate branches.

When interactions are nonreciprocal the modes are modified – they are described by Eq. (3) with nonzero right-hand side (r.h.s.) which is proportional to $\sigma_x^2 + \sigma_y^2$. The DL modes become coupled with each other and complex⁴³.

Now let us specify interparticle interactions. For the direct interaction between charged grains we naturally adopt the Yukawa potential which is characterized by (negative) particle charge Q and the screening length λ . For the wake we employ the commonly used simple model²⁹ of a point-like (positive) charge q located at the distance δ downstream each particle and also interacting with the neighboring particles via the Yukawa potential. The elements of the dynamical matrix (1) for such interactions are calculated in Appendix A, Eqs (A1) and (A2). For brevity, theoretical results in this paper are written in the dimensionless form – the frequency is normalized by the DL frequency scale,

$$\Omega_{\text{DL}} = \sqrt{\frac{Q^2}{m\lambda^3}},$$

and the wave vector is normalized by the lattice constant Δ : $\Omega/\Omega_{\text{DL}} \rightarrow \Omega$ and $\mathbf{k}\Delta \rightarrow \mathbf{k}$.

B. Types of mode coupling

After the normalization, the DL modes depend on three dimensionless parameters (along with the normalized wave vector): The screening parameter $\kappa = \Delta/\lambda$ as well as the relative wake charge $\tilde{q} = |q/Q|$ and distance $\tilde{\delta} = \delta/\Delta$. In experiments, κ is typically about unity whereas both wake parameters are usually small. Elements $\sigma_{x,y}$ [Eq. (A2)] are proportional to the product $\tilde{q}\tilde{\delta}$ and hence the coupling between the DL modes is very small [$\propto (\tilde{q}\tilde{\delta})^2$]. It becomes important only if different DL modes intersect (or they are very close to each other); otherwise the coupling can be neglected and then the modes can be treated independently, as described by Eq. (3). Let us elaborate on this point.

Behavior of two coupled modes, $\Omega_{1,2}(\mathbf{k})$, in a close proximity of their intersection can generally be described by the following equation:

$$[\Omega - \Omega_0 - \mathbf{U}_1 \cdot (\mathbf{k} - \mathbf{k}_0)][\Omega - \Omega_0 - \mathbf{U}_2 \cdot (\mathbf{k} - \mathbf{k}_0)] = \epsilon. \quad (4)$$

Here $\mathbf{U}_{1,2} = \partial\Omega_{1,2}/\partial\mathbf{k}$ are the group velocities of the two modes calculated at a point \mathbf{k}_0 of the intersection line $\Omega_0(\mathbf{k})$ (the latter is determined by the shape of the crossing modes) and ϵ characterizes the coupling. From Eq. (4) one readily concludes that the effect of the coupling critically depends on the sign of ϵ . This is illustrated in Fig. 2: When $\epsilon < 0$ the crossing modes merge and form a complex hybrid mode in a narrow range $|\mathbf{k} - \mathbf{k}_0| \propto \sqrt{\epsilon}$, with $\text{Re } \Omega_{\text{hyb}} \simeq \Omega_0 + \frac{1}{2}(\mathbf{U}_1 + \mathbf{U}_2) \cdot (\mathbf{k} - \mathbf{k}_0)$ and $\text{Im } \Omega_{\text{hyb}} \sim \pm\sqrt{\epsilon}$. Thus, one of the branches of the

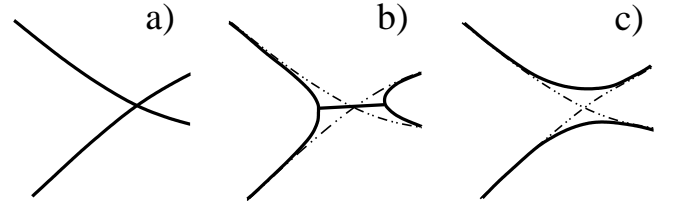


FIG. 2. Modification of coupled modes [Eq. (4)] in the vicinity of their crossing. The sketch depicts the modes in the $(\Omega, |\mathbf{k}|)$ -plane (a) in the absence of coupling, (b) with negative coupling ($\epsilon < 0$), and (c) with positive coupling ($\epsilon > 0$). Negative coupling results in the formation of a hybrid mode which can be unstable (see text); positive coupling causes the mode reconnection, while the modes remain stable and form a “forbidden band”.

hybrid mode has a positive imaginary part and hence can be unstable. When $\epsilon > 0$ the coupling is accompanied by reconnection (formation of a “forbidden band”) and the modes remain stable (real). Furthermore, the sign of the product $\mathbf{U}_1 \cdot \mathbf{U}_2$ in the unstable case determines the type of the instability, which is absolute for $\mathbf{U}_1 \cdot \mathbf{U}_2 < 0$ (the case illustrated in Fig. 2) and convective otherwise.

Now we can consider the DL modes described by Eqs (1) and (2), with the dispersion and coupling elements from Eqs (A1) and (A2). The detailed analysis shows that the intersection of the transverse in-plane mode $\Omega_{h\perp}(\mathbf{k})$ with the longitudinal in-plane, $\Omega_{h\parallel}(\mathbf{k})$, as well as with the out-of-plane mode $\Omega_v(\mathbf{k})$ is characterized by positive coupling and therefore is accompanied by reconnection illustrated in Fig. 2c, so that the modes remain stable. Moreover, the coupling for these two pairs of modes exactly disappears (Fig. 2a) if \mathbf{k} is parallel to one of the principal lattice axes (i.e., when $\theta = 0^\circ$ or 30° in Fig. 1a).

In contrast, for the remaining pair of $\Omega_v(\mathbf{k})$ and $\Omega_{h\parallel}(\mathbf{k})$ the coupling is *always negative*. As illustrated in Fig. 2b, this results in the formation of the *hybrid* mode with the imaginary part $\text{Im } \Omega_{\text{hyb}} \sim \pm\tilde{q}\tilde{\delta}$ (by the order of magnitude). If damping is low enough, this triggers the *mode-coupling instability*.

Thus, only the intersection between the out-of-plane and longitudinal in-plane modes is critical for stability of 2D plasma crystals⁴⁴.

C. Mode-coupling theory for 1D model

It is instructive to present a brief summary of the mode-coupling theory which was originally developed for a 1D string assuming the nearest-neighbor (NN) interactions^{31,32}. As it follows from the subsequent analysis (see Sec. III), this approach yields very simple expressions which can be conveniently implemented for practical purposes (e.g., to calculate the instability thresholds, see Sec. III D).

In the framework of 1D NN model³¹, the coupling be-

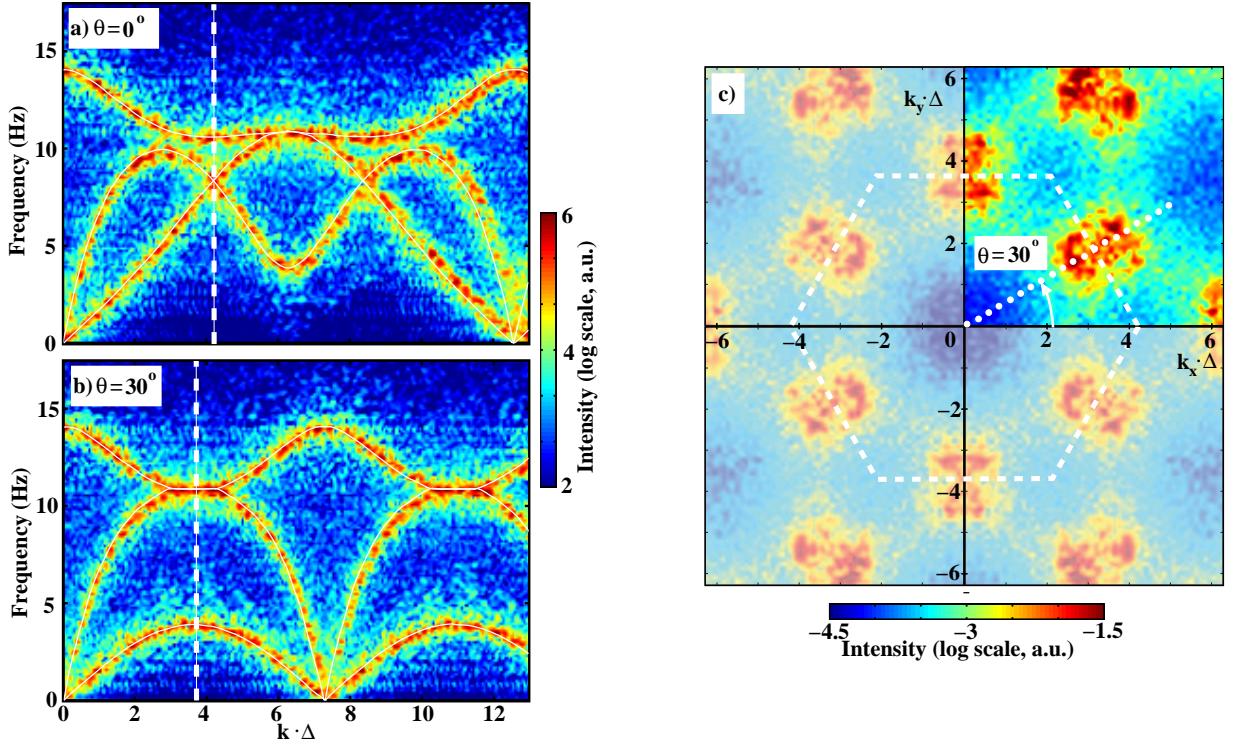


FIG. 3. Fluctuation spectra for “shallow” mode intersection (molecular dynamics simulations). Shown are the DL modes (positive branches) for \mathbf{k} at (a) $\theta = 0^\circ$ and (b) $\theta = 30^\circ$, and (c) spectrum in the \mathbf{k} -plane integrated over frequency (in the range between $10 \text{ Hz} \leq f \leq 14 \text{ Hz}$). Simulations are for $N = 16384$ particles of a mass $m = 6.1 \times 10^{-13} \text{ kg}$ and charge $Q = -18500 e$, the screening length is $\lambda = 600 \mu\text{m}$, the damping rate is $\nu = 0.87 \text{ s}^{-1}$. The horizontal and vertical confinements have eigenfrequencies $f_{\text{conf}}^{(h)} = 0.11 \text{ Hz}$ and $f_{\text{conf}}^{(v)} = 14.03 \text{ Hz}$, respectively. The lattice constant in the center is $\Delta \simeq 612 \mu\text{m}$ ($\kappa = \Delta/\lambda \simeq 1.02$). The wake parameters are $q = -0.2Q$ and $\delta = 0.3\lambda$. The dashed lines show the border of the first Brillouin zones, solid lines in (a) and (b) are theoretical curves. In (c) (as well as in other figures depicting spectra in the \mathbf{k} plane) the calculations for the upper right quadrant are mirrored in other three (shown in lighter colors).

tween horizontal (“longitudinal in-plane”) and vertical (“out-of-plane”) DL modes,

$$\begin{aligned}\Omega_h^2(k) &= 4(1 - \tilde{q}) (\kappa^{-1} + 2\kappa^{-2} + 2\kappa^{-3}) e^{-\kappa} \sin^2 \frac{1}{2}k, \\ \Omega_v^2(k) &= \Omega_{\text{conf}}^2 - 4(1 - \tilde{q}) (\kappa^{-2} + \kappa^{-3}) e^{-\kappa} \sin^2 \frac{1}{2}k,\end{aligned}\quad (5)$$

is described by the following (exact) equation:

$$(\Omega^2 - \Omega_h^2)(\Omega^2 - \Omega_v^2) + \sigma^2 = 0. \quad (6)$$

The range of k is limited by the first Brillouin zone $|k| \leq \pi$ (we use the same normalization as above), and the 1D coupling coefficient is

$$\sigma(k) = 2\tilde{q}\tilde{\delta} (\kappa^{-1} + 3\kappa^{-2} + 3\kappa^{-3}) e^{-\kappa} \sin k. \quad (7)$$

All characteristics of the hybrid mode (e.g., width, growth rate, etc.) can be easily derived from Eqs (5)-(7), see Appendix B.

These results are obtained in the limit of “small” $\tilde{\delta}$ (for general case, see Ref.³¹). In Sec. III D they will be compared with the exact 2D results derived in this limit.

D. Additional remarks

To conclude this Section, we should make two specific remarks which might be useful when considering DL waves and their coupling:

(i) The dynamical matrix D is solely characterized by interparticle interactions, i.e., does not depend on the damping rate ν . Thus, the *wave modes* $\Omega^2(\mathbf{k})$ – which are the eigenvalues of D – do not depend on ν either. As regards the *dispersion relations* $\omega(\mathbf{k})$, their dependence on ν is determined by the solutions of the quadratic equation $\omega(\omega + i\nu) - \Omega^2 = 0$. Therefore the effect of friction on waves is straightforward: For weakly damped waves (when $|\Omega| \gg \nu$, which is typical for experiments), one readily obtains $\omega(\mathbf{k}) \simeq \Omega(\mathbf{k}) - \frac{1}{2}i\nu$. From the practical point of view this implies that one can analyze undamped dispersion relations (i.e., put $\omega = \Omega$) and afterwards simply add $-\frac{1}{2}i\nu$ to the resulting imaginary part⁴⁵, which simultaneously identifies the instability threshold for the hybrid mode⁴⁶ (see Sec. III D 2).

(ii) For the analysis of wave modes in a crystal it is *sufficient* to consider the wave vectors from within the first Brillouin zone^{47,48} which is shown in Fig. 1b. This

zone is nothing but the Wigner-Seitz cell of the reciprocal lattice formed by the basis vectors \mathbf{b}_1 and \mathbf{b}_2 . Hence, the wave vectors \mathbf{k} and $\mathbf{k}' = \mathbf{k} + \mathbf{G}$ which are different by a linear combination of the basis vectors ($\mathbf{G} = m\mathbf{b}_1 + n\mathbf{b}_2$) are equivalent for wave modes, i.e., $\Omega(\mathbf{k} + \mathbf{G}) \equiv \Omega(\mathbf{k})$.

One has to remember this fact when analyzing dispersion relations at large $|\mathbf{k}|$. For instance, recently Liu *et al.*³⁶ identified one of the “hot spots” seen in their fluctuation spectra (in their Fig. 4c) as a new hybrid mode. This spot is centered at $|\mathbf{k}|\Delta \simeq 6.3 (\simeq 2\pi)$, $\theta = 0^\circ$ and therefore is located outside the first Brillouin zone; after the mapping with, say, $\mathbf{G} = \mathbf{b}_2$, its position is $|\mathbf{k}|\Delta \simeq \frac{2}{\sqrt{3}}\pi$, $\theta = 90^\circ$ (equivalent to 30° , see Fig. 1b; note also the change in the polarization, from the transverse to longitudinal). This naturally coincides with the position of the “regular” hybrid mode at the border of the first zone, whereas the “original” spot is merely its image outside it (as illustrated in Figs 3c and 4b).

III. FINGERPRINTS OF MODE COUPLING

In this Section we present detailed discussion and analysis of distinct fingerprints characterizing the wake-mediated coupling of DL modes in 2D crystals. Based on the results of Sec. II B we naturally focus only on the coupling between the out-of-plane and longitudinal in-plane modes, which causes the formation of the hybrid mode and can trigger the mode-coupling instability.

To illustrate key features of the mode coupling, the theoretical calculations were combined with the results of molecular dynamics (MD) simulations (see description in Appendix C). The DL wave modes were obtained from the simulations by plotting the so-called “fluctuation spectra” – intensity distributions of thermal velocity fluctuations in the (ω, \mathbf{k}) space.

A. Hybrid mode

Figure 3 represents a characteristic example of fluctuation spectra measured at the onset of the mode-coupling instability. It was obtained from MD simulations performed for the conditions close to those of experiment by Couédel *et al.*³⁴ (experiment II in Table I). In this case the out-of-plane and longitudinal in-plane modes are just barely touching. Such “shallow” intersection is nevertheless sufficient to form a distinct hybrid mode and to trigger the instability.

Figures 3a and b depict the DL modes in the $(\omega, |\mathbf{k}|)$ plane (positive branches). They are obtained for two directions of \mathbf{k} at $\theta = 0^\circ$ and $\theta = 30^\circ$, respectively (corresponding to the principal lattice axes, see Fig. 1a). Figure 3c shows the intensity distribution in the \mathbf{k} -plane (integrated over frequency), which provides a “top view” on the fluctuation spectra (dotted line shows the direction of $\theta = 30^\circ$). The hybrid mode can be identified in Figs 3b and c as “hot spots” located near the border of the first

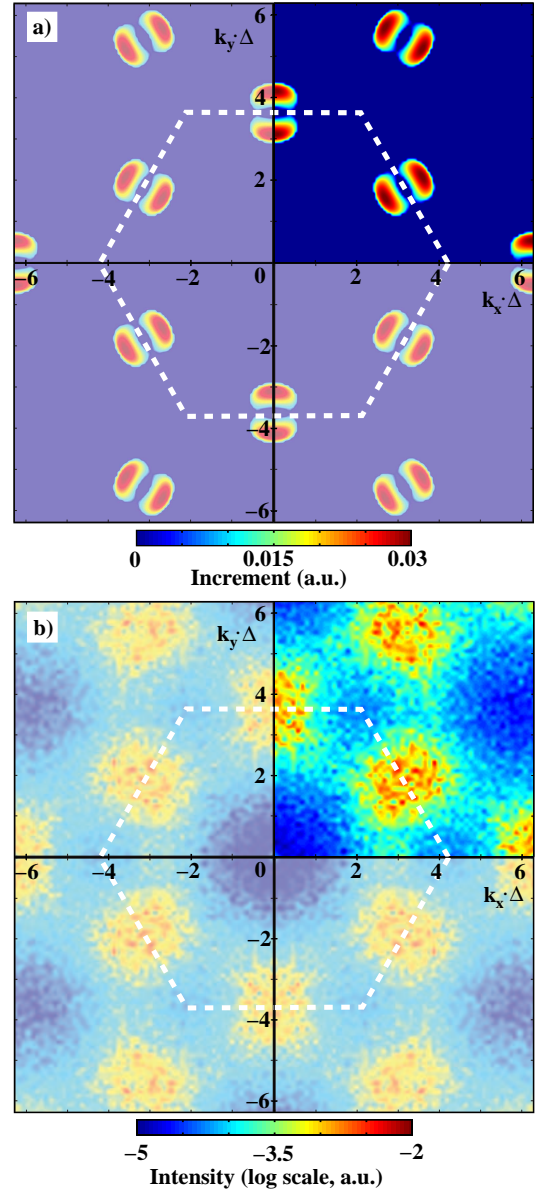


FIG. 4. (a) Contour plot of the growth rate $\text{Im } \omega_{\text{hyb}}(\mathbf{k})$ calculated from theory and (b) fluctuation spectra in the \mathbf{k} -plane obtained from simulations (integrated over frequency in the range between $10 \text{ Hz} \leq f \leq 14 \text{ Hz}$). To facilitate comparison with theory, the simulations are performed with periodic boundary conditions in the horizontal plane, otherwise the parameters are the same as in Fig. 3.

Brillouin zone, where the intersection occurs (note also images of the hybrid mode outside the first zone). The theoretical curves calculated from Eqs (1), (2), (A1), and (A2) for the same set of parameters demonstrate excellent agreement with simulations.

The reason why the fluctuation intensity is anomalously high at the position of the hybrid mode is the heating induced by the wake-mediated coupling. Figure 3 represents the marginally unstable regime, when $\text{Im } \omega_{\text{hyb}} (\simeq \text{Im } \Omega_{\text{hyb}} - \frac{1}{2}\nu) \gtrsim 0$. In this regime (also ob-

served in experiment³⁴) the effective growth rate of the instability is low, which allows us to obtain the fluctuation spectra before the crystal is eventually destroyed. It is worth noting, however, that the hybrid mode would usually appear as a “hot spot” even if the instability is suppressed by friction and $\text{Im } \omega_{\text{hyb}} < 0$. This is because the heating due to mode coupling is present also in stable regime. It becomes negligible only when $\text{Im } \Omega_{\text{hyb}} \ll \frac{1}{2}\nu$, and then the fluctuation intensity coincides with the intensity of DL modes outside the hybrid zone (where it is determined by the background neutrals or temperature of thermostat in simulations).

At the initial stage of the instability (and, of course, when the instability is suppressed) the effect of nonlinearity on the DL modes is not significant. In this case the contour plot of the growth rate $\text{Im } \omega_{\text{hyb}}(\mathbf{k})$ reasonably reproduces the distribution of fluctuation intensity in the vicinity of the hybrid mode. This is illustrated in Fig. 4 where we plotted $\text{Im } \omega_{\text{hyb}}(\mathbf{k})$ predicted by theory and the (frequency-integrated) fluctuation spectra from simulations. At a later stage, however, a nonlinear coupling between different modes becomes essential. This results in a variety of new phenomena, such as the energy cascades from the “hot spots” in the \mathbf{k} space and the generation of secondary harmonics at the double frequency of the hybrid mode (which are clearly seen in Fig. 3 of Ref.³⁴). Nevertheless, since the principal aim of this paper is to focus on distinct features of the *linear mode coupling*, we leave aside the discussion of numerous nonlinear coupling effects.

For the plots shown in Fig. 4 we used the same set of parameters as for Fig. 3, but for simulations we assumed periodic boundary conditions. The latter not only allowed us to directly compare the theory and simulations, but also to probe the effect of weak deviation from periodicity caused by the horizontal confinement. We see that the only noticeable difference between Figs 3c and 4b is the intensity of the hybrid mode. This reflects the fact that the growth rate of the instability critically depends on the interparticle distance Δ (resulting in exponentially growing difference in the heating at the initial stage). Therefore in the case of parabolic confinement (where Δ in the center is somewhat smaller than the average value) the intensity of the hybrid mode is higher than in the homogeneous case shown in Figs 4b. Otherwise, the positions and the overall shape of the “hot spots” in these two plots practically coincide, suggesting that weak inhomogeneity which is always present in experiments due to the horizontal confinement does not really affect the periodic structure of the Brillouin zones.

Finally, to illustrate the difference between “shallow” and “deep” intersections of the out-of-plane and longitudinal in-plane modes, in Fig. 5 we demonstrate the fluctuation spectra obtained for the eigenfrequency of vertical confinement $f_{\text{conf}}^{(v)}$ which is slightly lower than that in Fig. 3. This naturally shifts the out-of-plane mode down and thus makes the resulting hybrid mode much more pronounced: Figure 5 shows that for deep intersec-

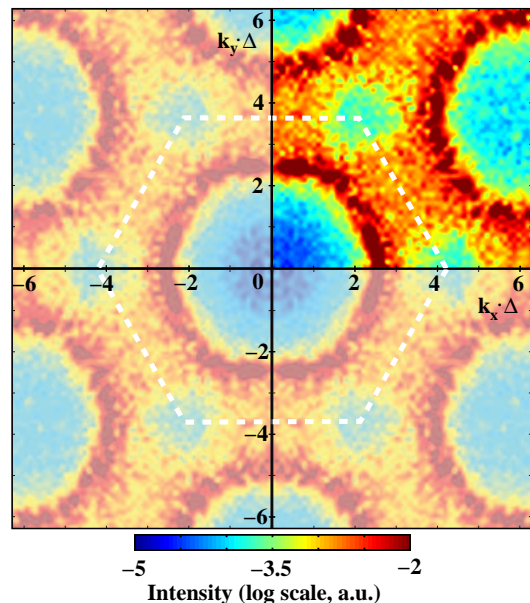


FIG. 5. Illustration of “deep” mode intersection (simulations). The eigenfrequency of the vertical confinement is $f_{\text{conf}}^{(v)} = 13.12$ Hz (spectra are integrated over frequency in the range between $9 \text{ Hz} \leq f \leq 13 \text{ Hz}$), the damping rate is $\nu = 2.19 \text{ s}^{-1}$. Otherwise the parameters are the same as in Fig. 3.

tions the separate “islands” of the hybrid mode merge into a joint broad “ring” (within the first Brillouin zone) and the “hot” region occupies substantially larger part of the \mathbf{k} -plane. The magnitude of $\text{Im } \Omega_{\text{hyb}}$ for deep intersections is usually much larger than for the shallow intersections and therefore the threshold conditions to trigger the mode-coupling instability in the former case are substantially relaxed (see discussion in Sec. III D). Note that in this case, in order to keep the crystal in the marginally unstable regime (which allows us to recover the fluctuation spectra) we increased the damping rate to $\nu = 2.19 \text{ s}^{-1}$.

B. Angular dependence

The dependence of DL modes on the direction of \mathbf{k} is evident from the discussion above. For the hybridization and the onset of the mode-coupling instability this dependence becomes crucial and therefore it deserves a separate discussion.

Figures 3 and 4 show that the first crossing of the out-of-plane and longitudinal in-plane modes always occurs at $\theta \simeq 30^\circ$, at the border of the first Brillouin zone. The area of the hybrid mode in the \mathbf{k} plane rapidly grows as the intersection gets deeper, and eventually the hybrid mode exists for any θ , as in Fig. 5. The crossing depth is controlled by changing the particle density or/and the eigenfrequency of the vertical confinement (see Sec. III D).

Therefore, when the DL fluctuation spectra are measured in experiments, under conditions close to the onset of hybridization (and, if not suppressed – of the mode-coupling instability), special attention should be paid to the orientation of \mathbf{k} with respect to the crystalline lattice. Under these circumstances the direction should be chosen according to the purpose of the experiment: If detection of the mode coupling is the goal, then $\theta = 30^\circ$ is the best choice; if unperturbed modes are to be measured, then $\theta = 0^\circ$ should be used. The experimental technique must therefore provide angular resolution, which is easily done for the in-plane modes, but is not always possible for the out-of-plane mode (since it is difficult to achieve angular positioning of the plasma crystal in an experiment). For instance, if the out-of-plane mode is measured with a fixed side-view camera³⁶ then the angle θ is set during the experiment and cannot be adjusted at the analysis stage, but if it is measured with a top-view camera (from the variation of individual particle intensity)³³ then θ -resolved wave spectra can be obtained.

C. Mixed polarization

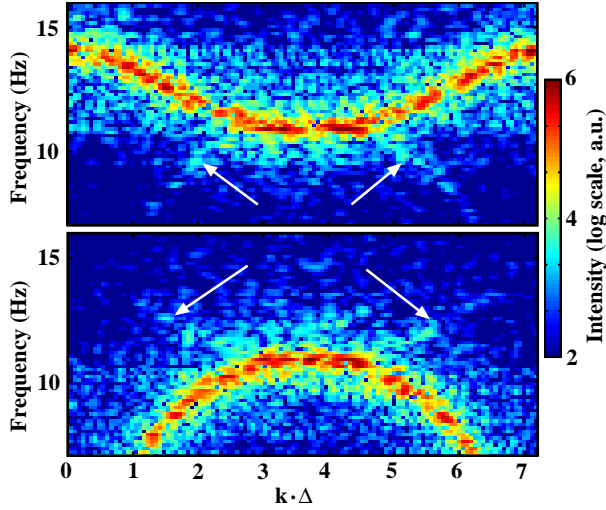


FIG. 6. Mixed polarization near the hybrid mode (simulations). Shown are the fluctuation spectra with the transverse out-of-plane (a) and longitudinal (b) polarization, for \mathbf{k} at $\theta = 30^\circ$ and parameters of Fig. 3. Arrows indicate traces of mixed polarization. Far from the hybrid mode (“hot spots”) the modes become purely out-of-plane (a) and in-plane (b).

As we pointed out in Sec. II, the DL wave modes are independent only when the wake-mediated coupling can be neglected: Far from the intersection or if the modes do not cross at all, the out-of-plane mode is purely transverse, one of the in-plane modes is longitudinal and the other is transverse. However, near the hybrid mode, where the coupling between the first two modes is strong, the theory predicts the emergence of *mixed polarization*³⁵: As the modes approach the junc-

tion point, their polarizations become *oblique* (in the plane formed by \mathbf{k} and the vertical axis), but the eigenvectors remain *mutually orthogonal*. At the point where they merge the polarization exhibits a discontinuity – the eigenvectors of the two modes form a single (hybrid) eigenvector with the elliptic polarization.

Traces of the mixed polarization for the out-of-plane mode have been observed in our recent experiment³⁴ (supplemental Fig. S2 therein) as well as in the experiment by Liu *et al.*³⁶ (shown in their Fig. 4b and erroneously interpreted as a “new mode”). In Fig. 6 we illustrate the mixed polarization observed in simulations (performed for the conditions of our experiment³⁴). The magnitude of this effect ($\propto \tilde{q}\tilde{\delta} < 1$) is quite small for typical experimental conditions, so that its detection requires very careful analysis and high signal-to-noise ratio.

D. Thresholds

The mode-coupling theory predicts two distinct thresholds: (i) *Confinement threshold*, which determines when the out-of-plane and longitudinal in-plane modes intersect; it depends on the combination of the vertical confinement frequency and the lattice constant (particle number density). This threshold identifies the sufficient condition for the hybrid mode to form, but only the necessary condition for the instability to set in. The sufficient condition for the instability is determined by (ii) *damping threshold* – this identifies the critical value of the damping rate (controlled by pressure) below which the instability is not suppressed. Let us discuss thresholds (i) and (ii) separately (we recall that all frequencies are normalized by Ω_{DL}).

1. Confinement threshold

The first intersection of the out-of-plane and longitudinal in-plane modes takes place at the border of the Brillouin zone³⁵, for \mathbf{k} at $\theta = 30^\circ$. Then, using the expressions for $\Omega_v(\mathbf{k})$ and $\Omega_{h\parallel}(\mathbf{k})$ we readily obtain the condition for the hybrid mode to form (confinement threshold),

$$\Omega_{\text{conf}} < \Omega_{\text{conf}}^{(\text{cr})} = \sqrt{\alpha_h + 2\alpha_v + |\beta|} \Big|_{\mathbf{k}=\mathbf{k}_{\text{cr}}}, \quad (8)$$

where $|\mathbf{k}_{\text{cr}}| = \frac{2}{\sqrt{3}}\pi$.

Generally, the critical confinement frequency $\Omega_{\text{conf}}^{(\text{cr})}$ is a rather complicated function of κ , $\tilde{\delta}$, and \tilde{q} ; it is given in Appendix D, Eq. (D1). However, Eq. (A1) suggests that to the accuracy $O(\tilde{\delta})$ the r.h.s. of Eq. (8) is independent of $\tilde{\delta}$ and is proportional to $\sqrt{1 - \tilde{q}}$. Thus, in this limit of “small” $\tilde{\delta}$ the combination $\Omega_{\text{conf}}^{(\text{cr})}/\sqrt{1 - \tilde{q}} \equiv \tilde{\Omega}_{\text{conf}}^{(\text{cr})}$ is a function of κ only (i.e., of the particle density) which is given by Eq. (D2). Figure 7a shows this universal

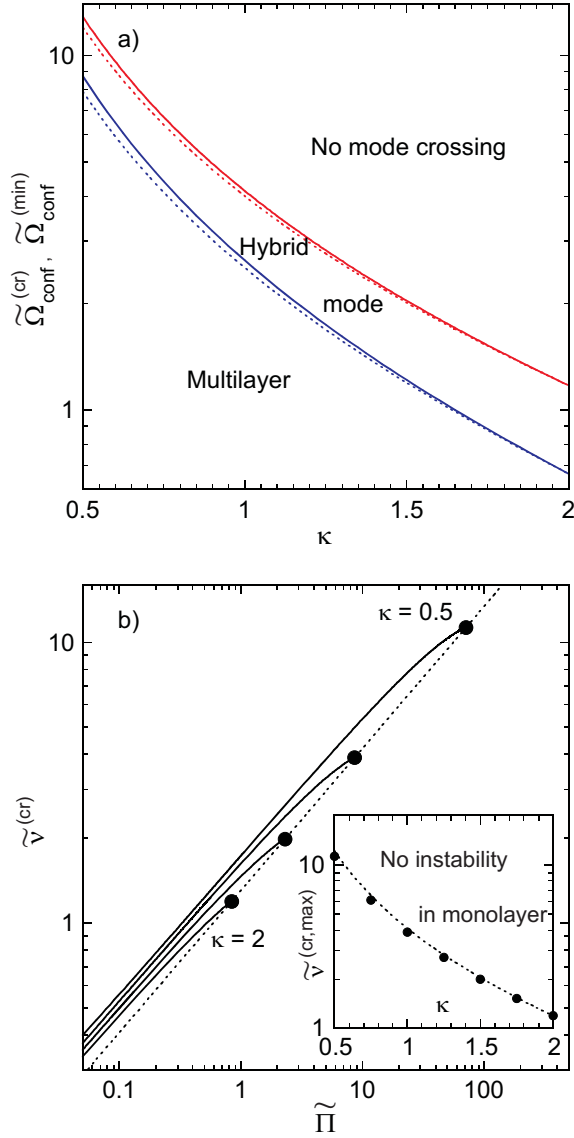


FIG. 7. Universal mode-coupling thresholds (limit of small $\tilde{\delta}$). (a) Critical value of the vertical confinement frequency, $\tilde{\Omega}_{\text{conf}}^{(\text{cr})}$ (confinement threshold, upper curves), which identifies the formation of the hybrid mode, shown versus the screening parameter $\kappa = \Delta/\lambda$. Also plotted is the minimum value $\tilde{\Omega}_{\text{conf}}^{(\text{min})}$ (below which only multilayer crystals can exist, lower curves). (b) Critical value of the damping rate, $\tilde{\nu}^{(\text{cr})}$ (damping threshold), which determines the sufficient condition for the instability to set in, shown versus the confinement control parameter, $\tilde{\Pi} = (\tilde{\Omega}_{\text{conf}}^{(\text{cr})})^2 - \tilde{\Omega}_{\text{conf}}^2$, for $\kappa = 0.5, 1, 1.5$, and 2 . The upper bound for the critical damping rate, $\tilde{\nu}^{(\text{cr,max})}$, is reached when $\tilde{\Omega}_{\text{conf}} = \tilde{\Omega}_{\text{conf}}^{(\text{min})}$ (marked by bullets). The inset in (b) shows $\tilde{\nu}^{(\text{cr,max})}$ for different κ , the mode-coupling instability is always suppressed above the dotted line. In both panels, solid lines are exact 2D results derived in this paper, dashed lines represent results of a 1D NN theory³¹. Tilde denotes universal normalization (see text for details).

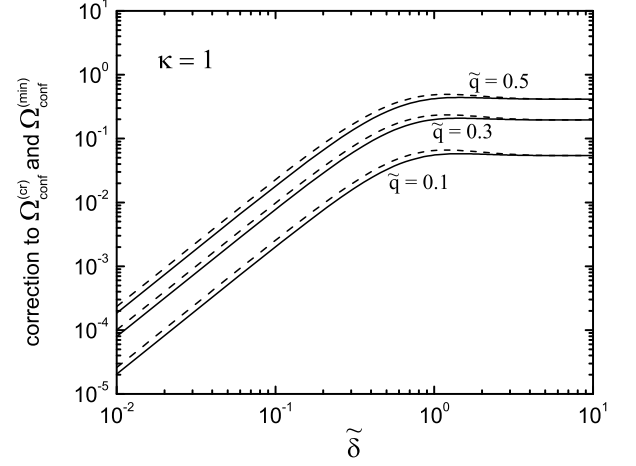


FIG. 8. Role of “finite” $\tilde{\delta}$. Shown is the relative deviation of $\tilde{\Omega}_{\text{conf}}^{(\text{cr})}$ (solid line) and $\tilde{\Omega}_{\text{conf}}^{(\text{min})}$ (dashed line) from the values calculated in the limit of small $\tilde{\delta}$ (see Fig. 7a). The results are illustrated for $\kappa = 1$ and three different values of \tilde{q} .

dependence in the useful range $0.5 < \kappa < 2$ (upper solid line).

One should always keep in mind that $\tilde{\Omega}_{\text{conf}}$ cannot be arbitrarily small^{31,32}: The out-of-plane mode $\tilde{\Omega}_v^2(\mathbf{k}) = \tilde{\Omega}_{\text{conf}}^2 - 2\alpha_v$ decreases monotonically with $|\mathbf{k}|$ and attains a minimum at the border of the first Brillouin zone. If $\tilde{\Omega}_v^2 < 0$ this formally implies instability. Physically, this is because the vertical confinement in this case becomes too weak to keep the particles in the monolayer and the bifurcation to a multilayer crystal occurs (i.e., a monolayer crystal is no longer a ground state). Thus, irrespective of the value of damping rate, a monolayer plasma crystal can only exist if the vertical confinement frequency exceeds the minimum value defined by⁴⁹

$$\tilde{\Omega}_{\text{conf}} > \tilde{\Omega}_{\text{conf}}^{(\text{min})} \simeq \sqrt{2\alpha_v}|_{\mathbf{k}=\mathbf{k}_{\text{cr}}} . \quad (9)$$

This value is given by Eqs (D3) and (D4) for arbitrary and small values of $\tilde{\delta}$, respectively. In the latter case we obtain a universal dependence $\tilde{\Omega}_{\text{conf}}^{(\text{min})}/\sqrt{1-\tilde{q}} \equiv \tilde{\Omega}_{\text{conf}}^{(\text{min})}$ on κ which is also plotted in Fig. 7a (lower solid line).

The effect of “finite” $\tilde{\delta}$ [i.e., beyond the accuracy $O(\tilde{\delta})$] is illustrated in Fig. 8 for $\kappa = 1$ (results are practically independent of κ in the range considered here). We plot the *relative deviations* of $\tilde{\Omega}_{\text{conf}}^{(\text{cr})}$ and $\tilde{\Omega}_{\text{conf}}^{(\text{min})}$ from the values given by Eqs (D2) and (D4), respectively. The deviations increase as $\propto \tilde{\delta}^2$ for $\tilde{\delta} \lesssim 0.3$ and then rapidly saturate at the level $(1-\tilde{q})^{-1/2} - 1$. [The latter is because both $\tilde{\Omega}_{\text{conf}}^{(\text{cr})}$ and $\tilde{\Omega}_{\text{conf}}^{(\text{min})}$ do not depend on the wake parameters for $\tilde{\delta} \gg 1$, whereas at $\tilde{\delta} \ll 1$ they scale as $\propto \sqrt{1-\tilde{q}}$.] Note that the curves have almost identical shape at different \tilde{q} , which indicates that the shown correction approximately scales as $\propto (1 - \sqrt{1-\tilde{q}})$. Given typical experimental errors (see Table I and Fig. 10), we conclude that the corrections shown in Fig. 8 can generally be neglected,

i.e., the accuracy of universal dependencies obtained in the limit of small $\tilde{\delta}$ is sufficient for practical purposes. In some cases, however, the effect of “finite” $\tilde{\delta}$ can nevertheless play an important role (see Sec. IV B).

Finally, let us compare the “exact” 2D results (in the limit of small $\tilde{\delta}$) with the results of approximate 1D NN mode-coupling theory summarized in Sec. II C. For the 1D case, the critical and minimum confinement frequencies are derived from Eq. (5) using the conditions $\Omega_h^2(\pi) = \Omega_v^2(\pi)$ and $\Omega_v^2(\pi) = 0$, respectively. For the comparison with the 2D results, we multiply the 1D results by constant “form factors” reflecting mismatch of 1D and 2D environments, which yields

$$\begin{aligned}\tilde{\Omega}_{\text{conf}}^{(\text{cr})} &\simeq 2F_{\text{conf}}^{(\text{cr})} \sqrt{(\kappa^{-1} + 3\kappa^{-2} + 3\kappa^{-3}) e^{-\kappa}}, \\ \tilde{\Omega}_{\text{conf}}^{(\text{min})} &\simeq 2F_{\text{conf}}^{(\text{min})} \sqrt{(\kappa^{-2} + \kappa^{-3}) e^{-\kappa}}.\end{aligned}\quad (10)$$

The form factors $F_{\text{conf}}^{(\text{cr})} = 1.25$ and $F_{\text{conf}}^{(\text{min})} = 1.49$ are determined from a fit to the 2D results, Eqs (D2) and (D4). The dependencies given by Eq. (10) are shown in Fig. 7a by dashed lines.

Thus, we see that the 1D NN theory provides excellent qualitative description of the confinement thresholds – even for small κ ; by multiplying these results with *constant* factors about unity we also get very good quantitative agreement with 2D results.

2. Damping threshold

As pointed out in Sec. II B, for $\theta = 30^\circ$ (as well as for 0°) the transverse in-plane mode becomes exactly decoupled. In this case the out-of-plane and longitudinal in-plane modes are governed by the following equation [similar to that for the 1D NN model, Eq. (6)]:

$$(\Omega^2 - \Omega_{h\parallel}^2)(\Omega^2 - \Omega_v^2) + \sigma_y^2 = 0.$$

In the vicinity of the intersection (Ω_0, \mathbf{k}_0) the coupled modes are described by Eq. (4) with $\epsilon \simeq (\sigma_y/2\Omega_0)^2$. The group velocities $\mathbf{U}_{h\parallel}$ and \mathbf{U}_v are collinear with \mathbf{k} due to the azimuthal symmetry at $\theta = 30^\circ$, so that the hybrid mode is given by

$$\begin{aligned}\Omega_{\text{hyb}}(\mathbf{k}) &= \Omega_0 + \frac{1}{2}(\mathbf{U}_{h\parallel} + \mathbf{U}_v) \cdot (\mathbf{k} - \mathbf{k}_0) \\ &\quad \pm \frac{1}{2}i\sqrt{\sigma_y^2(\mathbf{k}_0)/\Omega_0^2 - |\mathbf{U}_{h\parallel} - \mathbf{U}_v|^2|\mathbf{k} - \mathbf{k}_0|^2}.\end{aligned}$$

Thus, the width of the hybrid mode is $|\mathbf{k} - \mathbf{k}_0| = \sigma_y(\mathbf{k}_0)/(\Omega_0|\mathbf{U}_{h\parallel} - \mathbf{U}_v|)^{-1}$, and the maximum of $\text{Im } \Omega_{\text{hyb}}(\mathbf{k})$ is attained at the crossing point \mathbf{k}_0 . From this we immediately obtain the sufficient condition for the instability (damping threshold),

$$\nu < \nu^{(\text{cr})} = \sigma_y(\mathbf{k}_0)/\Omega_0, \quad (11)$$

where Ω_0 and \mathbf{k}_0 are determined from the crossing condition,

$$\Omega_0 = \sqrt{\alpha_h + \beta}\Big|_{\mathbf{k}=\mathbf{k}_0} = \sqrt{\Omega_{\text{conf}}^2 - 2\alpha_v}\Big|_{\mathbf{k}=\mathbf{k}_0}. \quad (12)$$

In order to relate Eq. (11) to the necessary instability condition [confinement threshold, Eq. (8)] we introduce the *confinement control parameter*,

$$\Pi = (\Omega_{\text{conf}}^{(\text{cr})})^2 - \Omega_{\text{conf}}^2,$$

which varies in the range from zero to $(\Omega_{\text{conf}}^{(\text{cr})})^2 - (\Omega_{\text{conf}}^{(\text{min})})^2$. It is obtained from Eq. (12),

$$\Pi = (\alpha_h + 2\alpha_v + \beta)|\mathbf{k}_0|^{\mathbf{k}_{\text{cr}}}, \quad (13)$$

where the r.h.s. is calculated as the difference at \mathbf{k}_{cr} and \mathbf{k}_0 . Thus, Eqs (11) and (13) determine the dependence of the critical damping rate $\nu^{(\text{cr})}$ on the control parameter Π via the parametric dependence on $|\mathbf{k}_0|$. For arbitrary $\tilde{\delta}$, this dependence is derived in Appendix D, Eqs (D5) and (D6).

Similar to the confinement threshold discussed in the previous subsection, for the damping threshold one can also obtain a universal dependence in the limit of small $\tilde{\delta}$. It is calculated in Eqs (D7) and (D8), where the r.h.s. are functions of κ only (along with the parameter $|\mathbf{k}_0|$) and the dependence on the wake parameters is explicitly given by the l.h.s. By introducing the universal normalization for the critical damping rate and the confinement control parameter,

$$\tilde{\nu}^{(\text{cr})} \equiv \frac{\sqrt{1-\tilde{q}}}{\tilde{q}\tilde{\delta}}\nu^{(\text{cr})}, \quad \tilde{\Pi} \equiv \frac{\Pi}{1-\tilde{q}}, \quad (14)$$

we conclude that $\tilde{\nu}^{(\text{cr})}$ is a universal function of κ and $\tilde{\Pi}$. Figure 7b shows $\tilde{\nu}^{(\text{cr})}$ versus $\tilde{\Pi}$ for four characteristic values of κ (solid lines). For “shallow” intersections, when Ω_{conf} is slightly below the critical value $\Omega_{\text{conf}}^{(\text{cr})}(\kappa)$ the critical damping rate increases as $\tilde{\nu}^{(\text{cr})} \propto \sqrt{\tilde{\Pi}}$, which can be readily derived from Eqs (D7) and (D8). Thus, for given κ and $\tilde{\Pi}$ (with $\Omega_{\text{conf}}^{(\text{min})} < \Omega_{\text{conf}} < \Omega_{\text{conf}}^{(\text{cr})}$) monolayer plasma crystals are unstable if $\nu < (\tilde{q}\tilde{\delta}/\sqrt{1-\tilde{q}})\tilde{\nu}^{(\text{cr})}(\kappa, \tilde{\Pi})$ and stable otherwise.

The critical damping rate is always bound from above, $\tilde{\nu}^{(\text{cr})} \leq \tilde{\nu}^{(\text{cr},\text{max})}$. For a given κ , the upper bound $\tilde{\nu}^{(\text{cr},\text{max})}(\kappa)$ corresponds to $\Omega_{\text{conf}} = \Omega_{\text{conf}}^{(\text{min})}(\kappa)$ and is marked by bullets in Fig. 7b. These points shown in the inset as a function of κ identify the *absolutely stable* region: The mode-coupling instability in monolayer crystals is always suppressed when ν exceeds $(\tilde{q}\tilde{\delta}/\sqrt{1-\tilde{q}})\tilde{\nu}^{(\text{cr},\text{max})}(\kappa)$.

According to the 1D NN theory [see Appendix B, Eq. (B1)] the critical damping rate is

$$\tilde{\nu}^{(\text{cr})} = \sqrt{\frac{\kappa^2 + 3\kappa + 3}{\kappa^2 + 2\kappa + 2}}\sqrt{\tilde{\Pi}},$$

i.e., it also scales as a square root of the control parameter. The upper bound for $\nu^{(\text{cr})}(\kappa)$ is obtained by substituting Eq. (10) for the maximum of Π , which yields

$$\tilde{\nu}^{(\text{cr},\text{max})} \simeq 2F^{(\text{cr},\text{max})}\sqrt{(\kappa^{-1} + 3\kappa^{-2} + 3\kappa^{-3}) e^{-\kappa}}, \quad (15)$$

TABLE I. Parameters of 2D crystals for different experiments (marked I to XII). The mode crossing is indicated as observed in that study.

	m (10^{-13} kg)	$ Q $ (e)	Δ (μm)	λ (μm)	κ	$f_{\text{conf}}^{(v)}$ (Hz)	ν (s^{-1})	ω_0 (s^{-1})	Mode crossing	$2\pi f_{\text{conf}}^{(v)}/\omega_0$	ν/ω_0
I ^{34‡}	6.1	17400	600	570	1.05	16.5	0.9	23.0	No	4.5	0.04
II ^{34‡}	6.1	18300	640	610	1.05	14.5	0.9	22.0	Yes	4.1	0.04
III ^{33‡}	5.3	14000	525	400	1.30	23.3	1.0	24.3	No	6.0	0.04
IV ^{33‡}	5.3	14200	514	514	1.00	20.5	1.0	25.4	No	5.1	0.04
V ^{33‡}	5.3	14600	1060	815	1.30	18.3	1.0	8.8	No	13.0	0.11
VI ^{33‡}	5.3	18000	600	600	1.00	16.3	1.1	25.6	Yes	4.0	0.04
VII ³⁶	4.2	9000	1000	700	1.40	13.9	3.5	6.7	No	13.0	0.52
VIII ³⁶	4.2	9000	600	700	0.86	13.9	3.5	14.4	Yes	6.1 [†]	0.24
IX ³⁷	4.2	12000	600	760	0.79	13.9	3.5	19.2	Yes	4.5	0.18
X ³²	5.5	15500	550	500	1.10	15.5	3.3	24.6	Yes	4.0	0.14
XI ⁴⁰	5.6	16000	700	930	0.75	16.0	1.2	17.6	No	5.7	0.07
XII ⁴⁰	5.6	13000	540	635	0.85	21.0	2.2	21.1	No	6.3	0.10

[†] The value is too high for the mode crossing (see Fig. 10), amended in Erratum³⁷.

[‡] For these data, error bars are available: $\pm 15\%$ for κ and λ , $\pm 10\%$ for $|Q|$, $\pm 8\%$ for $f_{\text{conf}}^{(v)}$, and $\pm 4\%$ for Δ .

where the corresponding form factor is $F^{(\text{cr,max})} = 1.28$. Equation (15), which is plotted in the inset of Fig. 7b by the dotted line, also provides excellent agreement with the 2D model. Hence, this is a convenient formula to identify conditions of absolute stability for a 2D crystal.

IV. COMPARISON WITH EXPERIMENTS

Wake-induced mode coupling has been observed in several experiments^{32–34,36}. However, the analysis of experimental results can be fastidious and needs to be done carefully. The fingerprints of the mode-coupling must be identified properly in order to avoid misinterpretations of the results. Therefore, in this Section we use the experiment of Ref.³⁴ as a characteristic example to demonstrate the principal features of the wake-induced mode coupling. Then, we give an overview of literature currently available on experiments with 2D crystals (stable and unstable)^{32–34,36,40}, the summary of experimental parameters is given in Table I. Finally, we discuss the stability of crystals in terms of thresholds introduced in the previous Section.

One of the most clear experimental evidence of mode-coupling in a 2D plasma crystal was reported in Ref.³⁴ (experiment II in Table I). A monolayer of microparticles was formed by levitating them in a plasma sheath above the lower rf electrode in a capacitively coupled discharge in a (modified) GEC chamber. The microspheres were made of melamine-formaldehyde and had a diameter of $9.19 \pm 0.09 \mu\text{m}$. The low argon pressure of 0.76 Pa ensured that the particle motion was only slightly damped. A high quality of the monolayer (with no detected particles above or below) was verified by using a side-view camera. Details of the experimental procedure are given

in Refs.^{33,34}.

The experimentally measured fluctuation spectra of two in-plane DL modes are shown in Fig. 9. Since this experiment was performed at conditions close to the onset of instability, all essential fingerprints of mode coupling are clearly visible:

- The mode coupling critically depends on the direction of the wave vector \mathbf{k} . The comparison of wave spectra calculated for $\theta = 0^\circ$ (Fig. 9a) and $\theta = 30^\circ$ (Fig. 9b) reveals that the onset of mode coupling first occurs at $\theta = 30^\circ$ – this results in the prominent “hot spots” in Fig. 9b. Colored red, they are almost two orders of magnitude more intense than the “normal” branches of the fluctuation spectra. The hot spot that lies within the first Brillouin zone (left one) represents the hybrid mode, the other one is its image in the higher Brillouin zone. These observations are in agreement with theory and complementary simulations (Fig. 3), which predicts that the mode coupling first takes place at $\theta = 30^\circ$ for “shallow” mode intersection.
- The less intense spot seen in Fig. 9a at $\theta = 0^\circ$ and $k\Delta \simeq 6.5$ is outside the first Brillouin zone (in Fig. 9c the location is along k_x -axis, at the right edge). As explained in Sec. IID, this spot should be mapped into the first Brillouin zone, where it represents the gap between two hot spots of the hybrid mode (in Fig. 9c, along the border of the Brillouin zone at $\theta \simeq 30^\circ$), and therefore its intensity is almost one order of magnitude smaller than the intensity of the hot spots.
- Traces of mixed polarization (out-of-plane mode) are clearly seen next to the hybrid mode in Figs. 9a and 9b. This gives a direct experimental proof that

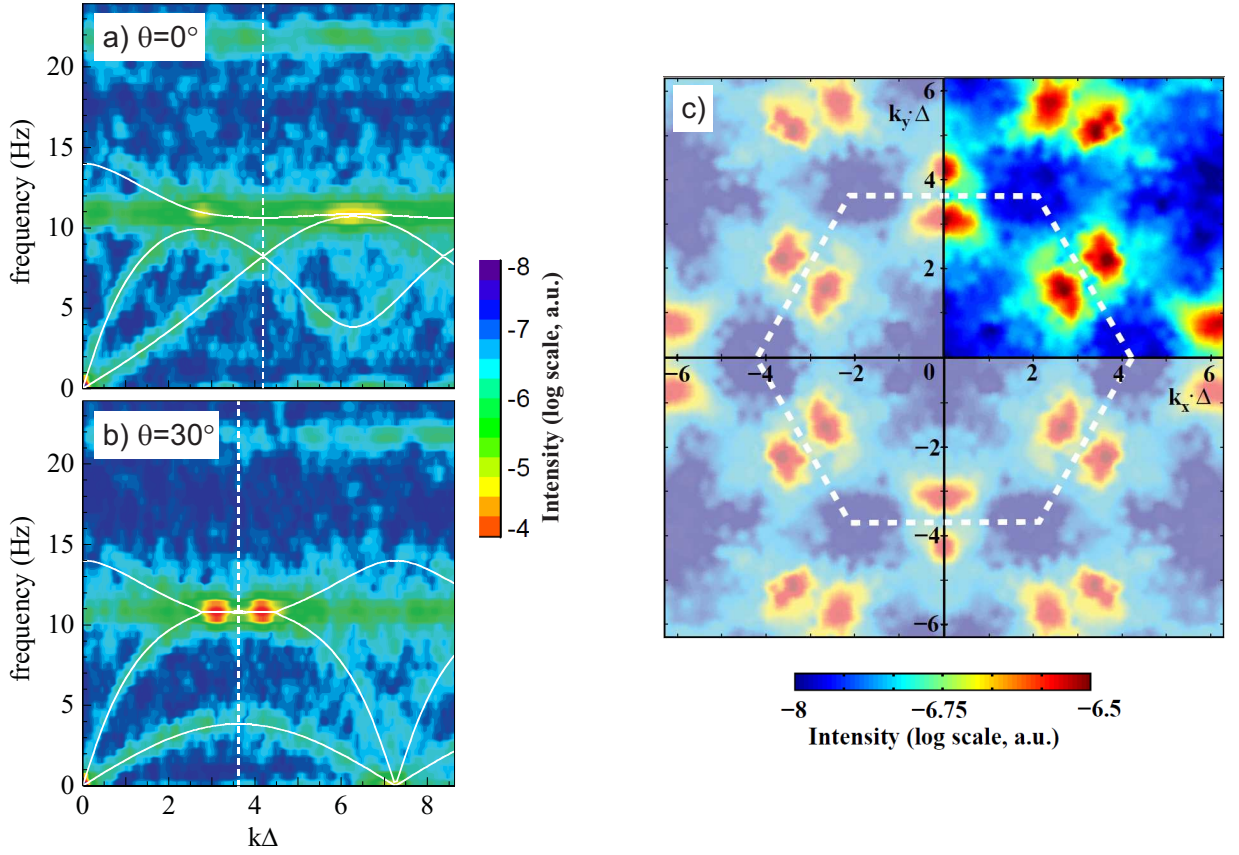


FIG. 9. In-plane fluctuation spectra for “shallow” mode intersection (experiment II³⁴ in Table I). Shown are the DL modes (positive branches) for \mathbf{k} at (a) $\theta = 0^\circ$ and (b) $\theta = 30^\circ$, and (c) spectrum in the \mathbf{k} -plane integrated over frequency (in the range between $10.5 \text{ Hz} \leq f \leq 14.5 \text{ Hz}$). The dashed lines show the border of the first Brillouin zones, solid lines in (a) and (b) are theoretical curves for all tree principal DL modes (assuming $\tilde{q} = 0.3$ and $\tilde{\delta} = 0.33$). Fluctuation spectra in (a) and (b) reveal clear traced of the out-of-plane mode (mixed polarization). In order to reduce noise in (c), the spectrum is an average of six spectra corresponding to equivalent directions in the crystal (using the invariance of hexagonal lattice to 60° rotations).

the out-of-plane mode becomes oblique close to the intersection point. A discrepancy of $\simeq 5\%$ between the experimentally measured in-plane projection of the out-of-plane mode and its theoretical dispersion relation can be explained by “finite- δ ” correction to the theory shown in Fig. 8 (which is about 4 % for the chosen values of wake parameters).

- Finally, all “hot spots” predicted by the theory and observed in simulations can be simultaneously seen in the experimental wave spectrum in \mathbf{k} -plane, which is shown in Fig. 9c.

Next, we analyze the stability of 2D plasma crystals in terms of the confinement threshold (which determines when the hybrid mode emerges). Available literature data on stable and unstable crystals is summarized in Table I, and the measured vertical confinement frequency $2\pi f_{\text{conf}}^{(v)}$ is compared to the theoretical threshold $\Omega_{\text{conf}}^{(\text{cr})}$ in Fig. 10. Note that for the comparison we change the normalization of $2\pi f_{\text{conf}}^{(v)}$: Instead of using Ω_{DL} – a natural frequency scale in theory, now we employ the 2D

analogue of dust plasma frequency,

$$\omega_0 = \sqrt{\frac{Q^2}{m\Delta^3}} \equiv \kappa^{-3/2} \Omega_{\text{DL}}.$$

This normalization allows us to minimize the experimental errors, since the interparticle distance is usually measured with much higher accuracy than the screening length (see footnote to Table I).

Figure 10 shows that all experiments listed in Table I as having no mode crossing are indeed represented by points well above the confinement threshold line. To the contrary, the points for experiments marked by mode crossing are located very close to the threshold line or below it. The only exception is the experiment VIII³⁶ by Liu *et al.*: The wake-induced mode coupling was clearly seen in the fluctuation spectra measured in³⁶, but the reported experimental parameters (yielding $2\pi f_{\text{conf}}^{(v)}/\omega_0 \simeq 6$, marked by green up triangle in Fig. 10) certainly do not allow the mode crossing, which indicates large measurement errors (amended in the subsequent Erratum³⁷). This example demonstrates that, by comparing experimental parameters to the theoretical confinement threshold near the

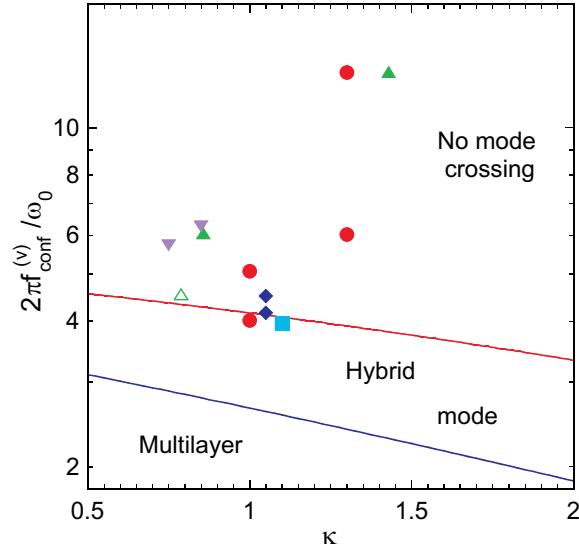


FIG. 10. Comparison of the vertical confinement frequency measured in experiments (Table I) with the theoretical confinement threshold (Fig. 7a): Blue diamonds are for experiments I and II, red circles for III-VI, green up triangles for VII and VIII, open green up triangle for IX, blue square for X, and purple down triangles for XI and XII. The vertical resonance frequency is normalized to $\omega_0 = \sqrt{Q^2/m\Delta^3}$. For experiments I to VI, error bars are available: $\pm 15\%$ for κ , $\pm 8\%$ for $f_{\text{conf}}^{(v)}$, and $\pm 12\%$ for ω_0 .

point where the hybrid mode (hot spot) emerges in the fluctuation spectra one can perform very sensitive consistency test for the deduced parameters.

A. Effective charge and wake parameters

At this point, let us briefly discuss the relation between the actual charge carried by particles and the effective charge which determines the dispersion properties of DL waves in 2D plasma crystals.

The common method to determine Q and λ in 2D crystals is to fit the measured fluctuation spectra for the in-plane modes by theoretical curves. The method is based on the *assumption* that the interparticle interaction potential can be approximated by the Yukawa form⁵⁰ and provides rather high accuracy. However, the dispersion relations are determined by the combined effect of direct interparticle interactions and the wake-mediated interactions. While the former contribution scales as $\propto Q^2$, the latter depends on a particular form of the wake. For the model of a point-like wake charge used in this paper the wake-mediated interactions scale as $\propto qQ$, which modifies the dispersion elements of the dynamical matrix (A1). In the limit of small $\tilde{\delta}$ (which turns out to be a remarkably accurate approximation, see Fig. 8) this yields the common renormalizing factor $(1 - \tilde{q})$ in Eq. (A1), and therefore the dispersion relations are determined by the *effective* charge $Q_{\text{eff}} = \sqrt{1 - \tilde{q}} Q$.

This fact should always be kept in mind when fitting the fluctuation spectra by theoretical dispersion relations: In theory, frequencies are normalized by $\Omega_{\text{DL}} \propto |Q|$ and hence the explicit dependence on the factor $(1 - \tilde{q})$ naturally disappears. This allows us, e.g., to directly compare the experimentally measured values of $2\pi f_{\text{conf}}^{(v)}/\omega_0$ with the theoretical confinement threshold without knowing the wake parameters (see Fig. 10).

Of course, the comparison of theory and experiments in terms of the damping threshold requires knowledge of \tilde{q} and $\tilde{\delta}$, since the growth rate of the hybrid mode is directly proportional to the effective “dipole moment” of wake $\tilde{q}\tilde{\delta}$. As was shown in Sec. IIID 2, in order to compare the measured value of ν/ω_0 (last column of Table I) with the theoretical damping threshold plotted in Fig. 7b, we need to know the factor $\tilde{q}\tilde{\delta}/(1 - \tilde{q})$ [see Eq. (14); additional factor $\sqrt{1 - \tilde{q}}$ in the denominator here is because ω_0 in experiments is determined by Q_{eff}]. In experiments, however, the wake parameters are generally unknown, so that a reasonable assumption should always be made in order to perform the analysis in terms of the damping threshold.

B. Effect of “finite” $\tilde{\delta}$

As we mentioned in Sec. IIID 2, under certain conditions the “finite- $\tilde{\delta}$ ” correction shown in Fig. 8 can become important. In particular, this happens in “marginal cases”, when the normalized value of the confinement frequency is very close to the corresponding threshold line (viz., when the distance to the line is comparable or less than the correction). For instance, such situation might occur for experiments II, VI, IX, and X shown in Fig. 10. However, typical experimental errors are relatively large, so that accounting for the corrections is hardly required in these cases.

As regards the comparison of theory with numerical simulations, where all input parameters are known precisely, the “finite- $\tilde{\delta}$ ” corrections can become crucial. To illustrate this, let us consider simulations of the shallow mode intersection shown in Fig. 3. The (normalized) confinement frequency in this case is $\simeq 1\%$ larger than $\tilde{\Omega}_{\text{conf}}^{(\text{cr})}$, i.e., according to the universal criterion for the confinement threshold the system is still marginally stable. However, by taking into account the correction to the confinement threshold from Fig. 8 (which is about $+4\%$ in this case) we conclude that the system is in fact marginally unstable – as observed in the simulations. In contrast, for the case of the deep mode intersection shown in Fig. 5 (where the confinement frequency is just $\simeq 6.5\%$ smaller) the correction plays practically no role.

V. CONCLUSIONS AND OUTLOOK

The theory of mode-coupling instability^{31,35} provides detailed picture of a *plasma-specific* melting scenario op-

erating in 2D plasma crystals. The melting associated with the wake-mediated coupling between the longitudinal in-plane and out-of-plane modes can only be triggered if (i) the modes intersect and (ii) the neutral gas damping is sufficiently low. Even if the instability is suppressed by the damping and the melting does not occur, the coupling always results in the formation of a hybrid mode which is revealed in fluctuation spectra by anomalous “hot spots” emerging at distinct positions in the \mathbf{k} -plane. In the vicinity of the hybrid mode, one can observe traces of mixed polarization for the two intersecting wave branches.

In this paper we showed that all these features can be considered as distinct fingerprints to identify the onset of the wake-induced mode coupling. This, in turn, allows us to determine certain combinations of the crystal parameters with a fairly good accuracy. For instance, the theory predicts a well-defined confinement threshold (for the ratio of the vertical confinement frequency to the dust-lattice frequency) at which the “hot spots” emerge. It is noteworthy that the effect of wakes on the dispersion relations is automatically taken into account via the charge renormalization, which yields the effective charge – the value which is deduced from the analysis of experimental fluctuation spectra.

On the other hand, the damping threshold as well as the evolution of the mode-coupling instability (if not suppressed) are determined by parameters of the wake – which are still poorly known for experiments. By identifying the onset of the instability and comparing it with the damping threshold derived above, one could obtain effective “dipole moment” of the wake. Furthermore, one could measure the energy growth rate at the initial instability stage and compare it with the theoretical prediction. Systematic studies in this direction would be highly desirable. However, we note that such measurements would only give us some mean characteristics of the wake, e.g., the first (“dipole”) moment in the multipole expansion.

We believe that future research into the stability of 2D plasma crystals should be focused, in particular, on the implementation of self-consistent wake models^{24,26,27} for the calculation of the mode coupling (which should also account for the spatial variation of the interaction parameters^{51,52}). Such studies will allow us to gain deeper insight into the plasma-specific mechanisms of melting operating in 2D systems and provide more reliable basis for future research into generic melting mechanisms.

Appendix A: Elements of dynamical matrix \mathbf{D} [Eq. (1)]

In Ref.³⁵ we calculated the elements of \mathbf{D} with the accuracy $O(\tilde{\delta})$. Although usually $\tilde{\delta}$ is small indeed, such a linear expansion might not be always sufficient for some experimental conditions (see Sec. IV B). Below we present the results for arbitrary $\tilde{\delta}$. For brevity, we introduce the

following auxiliary functions:

$$\begin{aligned}\Psi(x) &= (x^{-1} + x^{-2} + x^{-3})e^{-x}, \\ \Xi(x) &= (x^{-1} + 3x^{-2} + 3x^{-3})e^{-x}, \\ \Lambda(x) &= \frac{1}{2}[\Xi(x) - \Psi(x)].\end{aligned}$$

Then the dispersion elements of Eq. (1) are given by the following sums over integer m and n with excluded $(0, 0)$:

$$\begin{aligned}\alpha_h &= \sum_{m,n} \left\{ \Psi(\kappa s) - \tilde{q} \left[\Psi(\kappa s_\delta) - \tilde{\delta}^2 s_\delta^{-2} \Xi(\kappa s_\delta) \right] \right\} \\ &\quad \times \sin^2 \frac{1}{2} \mathbf{k} \cdot \mathbf{s}, \\ \alpha_v &= \sum_{m,n} \left\{ \Lambda(\kappa s) - \tilde{q} \left[\Lambda(\kappa s_\delta) - \tilde{\delta}^2 s_\delta^{-2} \Xi(\kappa s_\delta) \right] \right\} \\ &\quad \times \sin^2 \frac{1}{2} \mathbf{k} \cdot \mathbf{s}, \\ \beta &= \sum_{m,n} \left[\Xi(\kappa s) - \tilde{q} s^2 s_\delta^{-2} \Xi(\kappa s_\delta) \right] \\ &\quad \times (s_y^2 - s_x^2) s^{-2} \sin^2 \frac{1}{2} \mathbf{k} \cdot \mathbf{s}, \\ \gamma &= \sum_{m,n} \left[\Xi(\kappa s) - \tilde{q} s^2 s_\delta^{-2} \Xi(\kappa s_\delta) \right] s_x s_y s^{-2} \sin^2 \frac{1}{2} \mathbf{k} \cdot \mathbf{s}.\end{aligned}\tag{A1}$$

Here, the vector \mathbf{s} with the components $s_x = \frac{1}{2}m + n$ and $s_y = \frac{\sqrt{3}}{2}m$ and the absolute value $s = \sqrt{m^2 + mn + n^2}$ characterizes the relative positions of all neighbors in the hexagonal lattice; we also introduced $s_\delta = \sqrt{s^2 + \tilde{\delta}^2}$. The coupling elements are given by

$$\sigma_{x,y} = \tilde{q} \tilde{\delta} \sum_{m,n} \Xi(\kappa s_\delta) s_{x,y} s_\delta^{-2} \sin \mathbf{k} \cdot \mathbf{s}.\tag{A2}$$

In the NN approximation (formally applicable for $\kappa \gg 1$), the modes $\Omega_v^2(\mathbf{k})$ and $\Omega_{h||}^2(\mathbf{k})$ (whose coupling causes the hybridization) obtained from Eqs (A1) and (A2) coincide with Eqs. (5)-(7) for a 1D string. In the limits $\tilde{q} \rightarrow 0$ or $\tilde{\delta} \rightarrow \infty$, Eqs (A1) and (A2) reduce to conventional (wake-free) results for DL modes in 2D crystals. For $\tilde{\delta} \rightarrow 0$ and finite \tilde{q} one also obtains the wake-free results, but with the particle charge renormalized by the factor $\sqrt{1 - \tilde{q}}$.

Appendix B: Hybrid mode for 1D model

The intersection point between the horizontal and vertical modes, (Ω_0, k_0) , is readily derived from Eq. (5):

$$\Omega_0 = \sqrt{\frac{\kappa^2 + 2\kappa + 2}{\kappa^2 + 3\kappa + 3\tilde{\kappa}}} \Omega_{\text{conf}}, \quad \sin \frac{1}{2} k_0 = \frac{\Omega_{\text{conf}}}{\Omega_{\text{conf}}^{(\text{cr})}},$$

where $\Omega_{\text{conf}}^{(\text{cr})}$ is given by the first Eq. (10) with $F_{\text{conf}}^{(\text{cr})} = 1$. The maximum growth rate of the hybrid mode is obtained from Eq. (6),

$$\text{Im } \Omega_{\text{hyb}}(k_0) = \frac{\sigma(k_0)}{2\Omega_0},\tag{B1}$$

where $\sigma(k)$ is given by Eq. (7). This yields the critical damping rate $\nu^{(\text{cr})} = \sigma(k_0)/\Omega_0$.

Appendix C: Molecular dynamics simulations

The charged particles were confined in a vertical parabolic well with an eigenfrequency which was varied in the range of $15 \text{ Hz} < f_{\text{conf}}^{(\text{v})} < 25 \text{ Hz}$. In the horizontal plane, two options were investigated: parabolic confinement with an eigenfrequency $f_{\text{conf}}^{(\text{h})} < 0.5 \text{ Hz}$ and periodic boundary conditions (with $f_{\text{conf}}^{(\text{h})} = 0$). The equation of motion for each particle is

$$m\ddot{\mathbf{r}}_i + m\nu\dot{\mathbf{r}}_i = \sum_{j \neq i} \mathbf{F}_{ij} + \mathbf{C}_i + \mathbf{L}_i$$

where m is the particle mass, ν is the damping rate, \mathbf{r}_i the position of the i th particle, and $\mathbf{C}(\mathbf{r}_i)$ represents the confinement force. The force of interparticle interaction

is

$$\mathbf{F}_{ij} = -\frac{Q^2}{r_{ij}^2} \exp\left(-\frac{r_{ij}}{\lambda}\right) \left(1 + \frac{r_{ij}}{\lambda}\right) \frac{\mathbf{r}_{ij}}{r_{ij}} + \frac{Qq}{r_{w_{ij}}^2} \exp\left(-\frac{r_{w_{ij}}}{\lambda}\right) \left(1 + \frac{r_{w_{ij}}}{\lambda}\right) \frac{\mathbf{r}_{w_{ij}}}{r_{w_{ij}}}$$

where \mathbf{r}_{ij} is the distance from the particle i to the particle j , $\mathbf{r}_{w_{ij}}$ is the distance to the wake of the particle j , Q is the particle charge, and q is the point-like charge of the wake placed at a distance δ below each particle. The Langevin force is defined as

$$\langle \mathbf{L}_i(t) \rangle = \mathbf{0}, \quad \langle \mathbf{L}_i(t + \tau) \mathbf{L}_j(t) \rangle = 2\nu m T \delta_{ij} \delta(\tau),$$

where T is the temperature of the thermostat (here, δ is the Kronecker delta or the Dirac delta function).

In order to simulate systems of a size comparable to experimental (with $N \gtrsim 10^4$ particles) without any approximation (i.e., without cutoff radius in the interactions), the code was written in CUDA C and run on NVIDIA Tesla C1060 GPU or C2050 GPU computing cards. The equations of motion were solved using Beaman algorithm with predictor-corrector.

Appendix D: Calculation of thresholds for 2D model

To derive the confinement threshold, we substitute the dispersion elements from Eq. (A1) in Eq. (8) which yields

$$\Omega_{\text{conf}}^{(\text{cr})} = \sqrt{\sum_{m,n} \eta_m \left\{ (1+p) [\Xi(\kappa s) - \tilde{q} \Xi(\kappa s_\delta)] + \tilde{q} \tilde{\delta}^2 s_\delta^{-2} (3+p) \Xi(\kappa s_\delta) \right\}}. \quad (\text{D1})$$

Here the fact that $|\mathbf{k}_{\text{cr}}|s_y = m\pi$ is taken into account, so that it is convenient to introduce the parameter $\eta_m = \frac{1}{2} [1 - (-1)^m]$ (which is equal to 1 or 0 for odd or even m , respectively). Furthermore, for brevity we use $p \equiv s^{-2}(s_x^2 - s_y^2)$.

For the accuracy $O(\tilde{\delta})$, we can neglect in Eq. (D1) the second term in curly braces and set $s_\delta = s$, which results

in the following expression:

$$\frac{\Omega_{\text{conf}}^{(\text{cr})}}{\sqrt{1-\tilde{q}}} = \sqrt{\sum_{m,n} \eta_m (1+p) \Xi(\kappa s)}, \quad (\text{D2})$$

where the r.h.s. is a function of κ only. Thus, Eq. (D2) determine the universal dependence of $\Omega_{\text{conf}}^{(\text{cr})}$ on κ .

The minimum value of the confinement frequency defined in Eq. (9) is

$$\Omega_{\text{conf}}^{(\text{min})} = \sqrt{2 \sum_{m,n} \eta_m \left\{ \Lambda(\kappa s) - \tilde{q} \Lambda(\kappa s_\delta) + \tilde{q} \tilde{\delta}^2 s_\delta^{-2} \Xi(\kappa s_\delta) \right\}}, \quad (\text{D3})$$

for the accuracy $O(\tilde{\delta})$ it is reduced to

$$\frac{\Omega_{\text{conf}}^{(\text{min})}}{\sqrt{1-\tilde{q}}} = \sqrt{2 \sum_{m,n} \eta_m \Lambda(\kappa s)}. \quad (\text{D4})$$

For the damping threshold, we substitute the coupling element [Eq. (A2)] in Eq. (11) and the dispersion ele-

ments in Eqs (12) and (13). After some algebra we get

$$\nu^{(\text{cr})} = \frac{\tilde{q}\tilde{\delta} \sum_{m,n} s_\delta^{-2} s_y \Xi(\kappa s_\delta) \sin |\mathbf{k}_0| s_y}{\sqrt{\sum_{m,n} \left\{ \Psi(\kappa s) - \tilde{q}\Psi(\kappa s_\delta) + p [\Xi(\kappa s) - \tilde{q}\Xi(\kappa s_\delta)] + \tilde{q}\tilde{\delta}^2 s_\delta^{-2} (1+p) \Xi(\kappa s_\delta) \right\} \sin^2 \frac{1}{2} |\mathbf{k}_0| s_y}}, \quad (\text{D5})$$

$$\Pi = \sum_{m,n} (\eta_m - \sin^2 \frac{1}{2} |\mathbf{k}_0| s_y) \left\{ (1+p) [\Xi(\kappa s) - \tilde{q}\Xi(\kappa s_\delta)] + \tilde{q}\tilde{\delta}^2 s_\delta^{-2} (3+p) \Xi(\kappa s_\delta) \right\}. \quad (\text{D6})$$

For the accuracy $O(\tilde{\delta})$, we neglect the last terms in curly braces and set $s_\delta = s$. Then Eqs (D5) and (D6) are reduced to

$$\frac{\sqrt{1-\tilde{q}}}{\tilde{q}\tilde{\delta}} \nu^{(\text{cr})} = \frac{\sum_{m,n} s^{-2} s_y \Xi(\kappa s) \sin |\mathbf{k}_0| s_y}{\sqrt{\sum_{m,n} [\Psi(\kappa s) + p\Xi(\kappa s)] \sin^2 \frac{1}{2} |\mathbf{k}_0| s_y}}, \quad (\text{D7})$$

$$\frac{\Pi}{1-\tilde{q}} = \sum_{m,n} (\eta_m - \sin^2 \frac{1}{2} |\mathbf{k}_0| s_y) (1+p) \Xi(\kappa s), \quad (\text{D8})$$

where the r.h.s. depend only on κ and $|\mathbf{k}_0|$. Thus, Eqs (D7) and (D8) determine the universal dependence of the critical damping rate $\nu^{(\text{cr})}$ on the confinement control parameter Π via the parametric dependence on $|\mathbf{k}_0|$.

- ¹V. Fortov, A. Ivlev, S. Khrapak, A. Khrapak, and G. Morfill, *Physics Reports* **421**, 1 (2005).
- ²G. E. Morfill and A. V. Ivlev, *Rev. Mod. Phys.* **81**, 1353 (2009).
- ³B. I. Halperin and D. R. Nelson, *Phys. Rev. Lett.* **41**, 121 (1978).
- ⁴J. M. Kosterlitz and D. J. Thouless, *J. Phys. C: Solid State Physics* **6**, 1181 (1973).
- ⁵D. R. Nelson and B. I. Halperin, *Phys. Rev. B* **19**, 2457 (1979).
- ⁶A. P. Young, *Phys. Rev. B* **19**, 1855 (1979).
- ⁷S. T. Chui, *Phys. Rev. B* **28**, 178 (1983).
- ⁸C. A. Murray and D. H. Van Winkle, *Phys. Rev. Lett.* **58**, 1200 (1987).
- ⁹V. Nosenko, S. K. Zhdanov, A. V. Ivlev, C. A. Knapik, and G. E. Morfill, *Phys. Rev. Lett.* **103**, 015001 (2009).
- ¹⁰R. A. Quinn, C. Cui, J. Goree, J. B. Pieper, H. Thomas, and G. E. Morfill, *Phys. Rev. E* **53**, R2049 (1996).
- ¹¹T. E. Sheridan, *Phys. Plasmas* **16**, 083705 (2009).
- ¹²T. E. Sheridan, *Phys. Plasmas* **15**, 103702 (2008).
- ¹³K. Zahn and G. Maret, *Phys. Rev. Lett.* **85**, 3656 (2000).
- ¹⁴I. V. Schweigert, V. A. Schweigert, A. Melzer, and A. Piel, *Phys. Rev. E* **62**, 1238 (2000).
- ¹⁵S. Nunomura, S. Zhdanov, D. Samsonov, and G. Morfill, *Phys. Rev. Lett.* **94**, 045001 (2005).
- ¹⁶S. Nunomura, T. Misawa, N. Ohno, and S. Takamura, *Phys. Rev. Lett.* **83**, 1970 (1999).
- ¹⁷G. Morfill, A. V. Ivlev, and J. R. Jokipii, *Phys. Rev. Lett.* **83**, 971 (1999).
- ¹⁸O. S. Vaulina, S. A. Khrapak, A. P. Nefedov, and O. F. Petrov, *Phys. Rev. E* **60**, 5959 (1999).
- ¹⁹O. Ishihara and S. V. Vladimirov, *Phys. Plasmas* **4**, 69 (1997).
- ²⁰O. Ishihara, *Phys. Plasmas* **5**, 357 (1998).

- ²¹S. V. Vladimirov and A. A. Samarian, *Phys. Rev. E* **65**, 046416 (2002).
- ²²S. V. Vladimirov, S. A. Maiorov, and O. Ishihara, *Phys. Plasmas* **10**, 3867 (2003).
- ²³Lampe, M., G. Joyce, G. Ganguli, and V. Gavrilchaka, 2000, *Phys. Plasmas* **7**, 3851.
- ²⁴L.-J. Hou, Y.-N. Wang, and Z. L. Mišković, *Phys. Rev. E* **64**, 046406 (2001).
- ²⁵W. J. Miloch, J. Trulsen, and H. L. Pécseli, *Phys. Rev. E* **77**, 056408 (2008).
- ²⁶R. Kompaneets, U. Konopka, A. V. Ivlev, V. Tsytovich, and G. Morfill, *Phys. Plasmas* **14**, 052108 (2007).
- ²⁷R. Kompaneets, S. V. Vladimirov, A. V. Ivlev, and G. Morfill, *New J. Phys.* **10**, 063018 (2008).
- ²⁸A. Melzer, V. A. Schweigert, and A. Piel, *Phys. Rev. Lett.* **83**, 3194 (1999).
- ²⁹A. Melzer, V. A. Schweigert, I. V. Schweigert, A. Homann, S. Peters, and A. Piel, *Phys. Rev. E* **54**, R46 (1996).
- ³⁰G. Joyce, M. Lampe, and G. Ganguli, *Phys. Rev. Lett.* **88**, 095006 (2002).
- ³¹A. V. Ivlev and G. Morfill, *Phys. Rev. E* **63**, 016409 (2001).
- ³²A. V. Ivlev, U. Konopka, G. Morfill, and G. Joyce, *Phys. Rev. E* **68**, 026405 (2003).
- ³³L. Couëdel, V. Nosenko, S. K. Zhdanov, A. V. Ivlev, H. M. Thomas, and G. E. Morfill, *Phys. Rev. Lett.* **103**, 215001 (2009).
- ³⁴L. Couëdel, V. Nosenko, A. V. Ivlev, S. K. Zhdanov, H. M. Thomas, and G. E. Morfill, *Phys. Rev. Lett.* **104**, 195001 (2010).
- ³⁵S. K. Zhdanov, A. V. Ivlev, and G. E. Morfill, *Phys. Plasmas* **16**, 083706 (2009).
- ³⁶B. Liu, J. Goree, and Y. Feng, *Phys. Rev. Lett.* **105**, 085004 (2010).
- ³⁷B. Liu, J. Goree, and Y. Feng, *Phys. Rev. Lett.* **105**, 269901 (2010).
- ³⁸D. H. E. Dubin, *Phys. Rev. Lett.* **71**, 2753 (1993).

- ³⁹K. Qiao and T. W. Hyde, Phys. Rev. E **68**, 046403 (2003).
- ⁴⁰D. Samsonov, S. Zhdanov, and G. Morfill, Phys. Rev. E **71**, 026410 (2005).
- ⁴¹S. V. Vladimirov, P. V. Shevchenko, and N. F. Cramer, Phys. Rev. E **56**, R74 (1997).
- ⁴²S. V. Vladimirov, V. V. Yaroshenko, and G. E. Morfill, Phys. Plasmas **13**, 030703 (2006).
- ⁴³Matrix D is symmetric and hence can be reduced to the diagonal form also for $\sigma_{x,y} \neq 0$, but with complex eigenvalues.
- ⁴⁴For 2D plasma crystals, the “trivial” origin of the non-Hamiltonian behavior associated with neutral gas friction can often be neglected, since the corresponding damping rate is typically one-to-two orders of magnitude smaller than the Einstein frequency².
- ⁴⁵The real part of the dispersion relations remains unaffected by damping. This is only violated for the acoustic modes $\Omega_{h\parallel,\perp}(\mathbf{k})$ in a close proximity of $\mathbf{k} = \mathbf{0}$ and therefore is unimportant for the analysis.
- ⁴⁶This also shows that the analysis of wave modes does not require any distinction in terms of friction, as it has been done by Liu *et al.*³⁶ (where our previous theoretical results^{31,32,35} were erroneously referred to as “frictionless”).
- ⁴⁷C. Kittel, *Introduction to Solid State Physics*, edited by Wiley (Wiley, New York, 1961).
- ⁴⁸E. M. Lifshitz and L. P. Pitaevskii, *Physical Kinetics*, edited by Pergamon (Pergamon, Oxford, 1981).
- ⁴⁹ $\Omega_v^2(\mathbf{k})$ is practically independent of θ at the border of the Brillouin zone³⁵ (the variation is $\lesssim 1\%$), so that in order to facilitate the calculations we substitute \mathbf{k} at $\theta = 30^\circ$.
- ⁵⁰The functional form of the interaction potential can deviate from the Yukawa dependence at large distances, but within several λ this deviation is negligible indeed (see Ref.²⁶).
- ⁵¹V. V. Yaroshenko, A. V. Ivlev, and G. E. Morfill, Phys. Rev. E **71**, 046405 (2005).
- ⁵²R. Kompaneets, A. V. Ivlev, V. Tsytovich, and G. Morfill, Phys. Plasmas **12**, 062107 (2005).